SIMULATION OF MONSOON BOUNDARY-LAYER PROCESSES USING A REGIONAL SCALE NESTED GRID MODEL

KIRAN ALAPATY, SETHU RAMAN and R. V. MADALA*

Department of Marine, Earth and Atmospheric Sciences, North Carolina State University, N.C. 27695-8208, U.S.A

(Received in final form 21 June, 1993)

Abstract. A nested grid regional model with a high vertical resolution in the atmospheric boundary layer is used to simulate various atmospheric processes during an active monsoon period. A turbulence kinetic energy closure scheme is used to predict the boundary-layer structure. Model predictions indicate different structures of the boundary layer over land and oceans, as observed. Significant diurnal variation in boundary-layer structure and associated processes is predicted over land and negligible variations over oceans. The Somali jet over the Arabian Sea is well predicted. Location of the predicted monsoon depression and the associated rainfall are in good agreement with the observations. Also, predicted rainfall and its spatial distribution along the west coast of India are in good agreement with the observations.

1. Introduction

It is well known that atmospheric boundary-layer (ABL) processes play an important role on the dynamics and the thermodynamics of the atmosphere. Mesoscale models using higher order closure techniques for boundary-layer physics showed better performance in predicting mean ABL structure (e.g., Deardorff, 1980; Yamada and Mellor 1975; Sun and Hsu, 1988; Huang Raman, 1989; Holt and Raman, 1990). Numerical studies (Holt and Raman, 1988) indicate that the turbulent kinetic energy-dissipation (TKE-ϵ) closure is preferable to first-order closure in predicting turbulence structure of the ABL. A sensitivity study of a numerical model to various boundary-layer parameterizations (Holt *et al.*, 1990) indicates that the mesoscale structure of the winds, temperature and moisture are more accurately predicted with the higher order turbulence closure. Holt *et al.* (1990) also found that increased vertical resolution in the ABL without better boundary-layer physics showed no improvement in model predictions.

Monsoon weather is characterized by the presence of strong low-level westerly flow. Boundary-layer processes over this region are complex due to the presence of the low-level Somali jet over the Arabian Sea and convective processes associated with orographic lifting of moist air along the west coast of India. Observational studies of the mean structure of the marine boundary layer over the Arabian sea (Holt and Raman, 1985, 1987) during MONEX 79 indicate that the

* Naval Research Laboratory, Washington, D.C., 20375, U.S.A.

Boundary-Layer Meteorology **67**: 407–426, 1994.

monsoon boundary layer is affected by the large-scale flow. Over regions of cumulus activity, Holt and Raman (1985, 1987) found that the prevailing Somali jet structure is depressed in height. It was also found that (Holt and Raman, 1987) latent heat fluxes over the Arabian Sea during the active monsoon conditions are about two to three times larger than those during the "break" conditions and that sensible heat fluxes increased considerably during the monsoon onset as compared to premonsoon conditions.

The objective of this paper is to simulate the monsoon circulations and associated processes using a sophisticated boundary-layer parameterization scheme with high vertical resolution in the ABL. We also examine boundary-layer structure over land and over the adjacent oceans during an active monsoon period and compare the results with observations.

2. Model Description

The present study utilizes a nested grid model developed at the Naval Research Laboratory and North Carolina State University based on the limited area dynamical weather prediction model developed earlier by Madala *et al.* (1987). It is a primitive equation model written in a pressure-based σ-coordinate system having a one-way interacting nested grid network. The σ-coordinate is defined by $\sigma = p/p_s$, where p is the pressure and p_s the surface pressure. Various physical processes are included either explicitly or in parameterized form. The model physics includes latent heat, sensible heat, and momentum exchange between the ABL and the underlying surface, grid-scale precipitation, dry convection, and diffusion processes. (Boundary-layer parameterization used in the model is described in the following section.) The cumulus parameterization scheme suggested by Kuo (1974) and Anthes (1977) is used in the model. Short- and long-wave radiative processes are not included in the present model. Second-order diffusion for momentum on σ-surfaces and for heat and water vapor on p-surfaces is used to account for the cascading of energy into unresolved subgrid-scale waves. If super-saturation exists at any level, the excess moisture is assumed to condense and fall out to the next lower layer and evaporate or continue to fall depending upon the degree of saturation at that level. The model has a dry convective adjustment procedure to remove dry convective instability that can occur during model integration.

The time integration scheme utilized in the present model is a split-explicit method which allows a larger time step by effectively separating various terms in the prognostic equations into parts governing slow-moving Rossby modes and fast-moving gravity modes. For the first and second fast-moving gravity modes, a smaller time step is used than for all other modes. The implementation of these varying time steps is the basis for the split-explicit method. The time steps for the slow moving modes in the CGM (Coarse-Grid Mesh) and the FGM (Fine-Grid Mesh) are 300 and 100 s, respectively, and appropriate smaller time steps are used for the fast-moving modes. For further details, the reader is referred to Madala

et al. (1987). For the horizontal differencing, a staggered grid network (Arakawa C-grid) is used with p_s, q, T, ϕ, $\dot{\sigma}$ specified at the same horizontal points, and u and v interlaced between them where p_s is the surface pressure, q the specific humidity, T the temperature, ϕ the geopotential, $\dot{\sigma}$ the vertical velocity of σ, u the zonal wind velocity, and v the meridional wind velocity. The finite difference technique used is second-order accurate. It conserves total energy, mass, and momentum in the absence of heat and momentum sources.

Model topography was obtained from the navy 10′ global topography data for 1.5° and 0.5° horizontal resolutions. Model sea surface temperatures (SST) were obtained from the 1° resolution global climatological values based on a 10 year average for the month of July. The Davies scheme (1976, 1983) is employed to provide lateral boundary conditions in the present version of the model. For any independent variable a, it can be written as, $a = (1 - \alpha)a_m + \alpha a_b$, where the subscript m represents model-computed values and the subscript b represents the boundary values obtained either from observations or from a coarser version of the model. The merging is done over six points at the boundaries of both domains. The α is defined as a quadratic function of the minimum distance from the lateral boundary in units of the grid spacing (Gronas *et al.*, 1987). At each time step, the boundary values a_b for the coarse grid are obtained through a linear interpolation in time from the ECMWF data. For the FGM domain, lateral boundary conditions a_b are obtained through a linear interpolation in time and space from the CGM domain. At the model top and bottom, the boundary condition for $\dot{\sigma}$ is zero.

2.1. Boundary-layer parameterization

The atmosphere up to about 850 hPa is divided into seven nonuniform layers as shown in Table I. The surface boundary layer is parameterized based on similarity theory (Monin and Yaglom, 1971) and the nondimensional functions can be written as,

$$\frac{kz}{u_*}\frac{\partial u}{\partial z} = \phi_m(z/L)\,,$$

$$\frac{kz}{\theta_*}\frac{\partial \Theta}{\partial z} = \phi_h(z/L)\,, \tag{1}$$

$$\frac{kz}{q_*}\frac{\partial q}{\partial z} = \phi_q(z/L)\,,$$

where the nondimensional stability parameters ϕ_m, ϕ_h and ϕ_q for momentum, heat and moisture are functions of the Monin–Obukhov length, L (Businger *et al.*, 1971). In the mixed layer, the coefficient of vertical eddy diffusion is determined by the prognostic calculation of turbulence kinetic energy and its dissipation rates using the E–ϵ closure technique (Holt and Raman, 1988) with the constants

TABLE I

Model σ levels and corresponding pressures for a surface at 1000 hPa

Model level	Sigma and pressure levels	
K	σ	p (hPa) (Approx)
1	0.05	50
2	0.15	150
3	0.25	250
4	0.35	350
5	0.45	450
6	0.55	550
7	0.65	650
8	0.75	750
9	0.82	820
10	0.86	860
11	0.90	900
12	0.935	935
13	0.96	960
14	0.9775	977
15	0.99	990
16	0.9975	997

suggested by Detering and Etling (1985). Prognostic equations for turbulence kinetic energy (E) and its dissipation (ϵ) can be written as:

$$\frac{\partial E}{\partial t} = -\overline{u'w'}\frac{\partial u}{\partial z} - \overline{v'w'}\frac{\partial v}{\partial z} + \frac{g}{\Theta}\overline{w'\theta'} - \\ - \frac{\partial}{\partial z}\left(\overline{w'E} + \frac{\overline{p'w'}}{\rho}\right) - \epsilon, \tag{2}$$

$$\frac{\partial \epsilon}{\partial t} = \frac{c_1\epsilon}{E}\left(-\overline{u'w'}\frac{\partial u}{\partial z} - \overline{v'w'}\frac{\partial v}{\partial z} + \frac{g}{\Theta}\overline{w'\theta'}\right) - \\ - \frac{c_2\epsilon^2}{E} + c_3\frac{\partial}{\partial z}\left(K_m\frac{\partial \epsilon}{\partial z}\right), \tag{3}$$

where $\overline{u'w'}$ and $\overline{v'w'}$ are turbulence fluxes of momentum, ρ the density, p' the fluctuating pressure, and K_m the eddy exchange coefficient. The first two terms on the right hand side (rhs) of (2) represent shear production, the third, buoyancy production, fourth, turbulence transport and the fifth, the dissipation. The three terms on the rhs of (3) represent the production, destruction, and the vertical transport of turbulent kinetic energy dissipation, respectively.

2.2. Ground temperature

The ground temperature T_g is predicted by a soil slab model (Blackadar, 1976), which predicts ground temperature, based on the surface energy equation (Chang, 1979):

$$\frac{\partial T_g}{\partial t} = \frac{I}{C_g} + \omega(T_m - T_g) + \frac{\rho c_p}{C_g}(\overline{w'\theta'})_0 , \tag{4}$$

where I is the net radiation, C_g the heat capacity per unit area of soil slab, ω the inverse of the time scale for heat conduction in the soil (2π/1 day), T_m the deep soil temperature, c_p the specific heat of air, and $(\overline{w'\theta'})_0$ is the kinematic heat flux defined as:

$$(\overline{w'\theta'})_0 = -u_* T_* . \tag{5}$$

The terms on the rhs of (4) represent net radiation, soil heat flux and surface turbulent heat flux, respectively. Net radiation I is the sum of incoming solar radiation absorbed at the surface I_S, atmospheric longwave back-scattering radiation I_L and outgoing longwave surface radiation O_L. Incoming solar radiation is estimated as:

$$I_S = S \cos Z(1 - A)b^{\sec Z} , \tag{6}$$

where S is the solar constant, Z the solar zenith angle, b the atmospheric turbidity, which is a function of precipitation rate, and A the surface albedo which is assumed as 0.28 over land and 0.08 over water. Water vapor is not considered in the relationship for net longwave radiation computed using Brunt's equation (Seller, 1965):

$$I_L - O_L = -\epsilon_m(1 - 0.61)\beta T_g^4 , \tag{7}$$

where e_m is soil emissivity (0.7) and β is the Stefan–Boltzmann constant. Heat capacity of the soil slab C_g is approximated as an 80 m deep air layer (Chang, 1979).

2.3. Simulation domain, initial conditions and numerical experiments

The domain of simulation in the Coarse-Grid Mesh (CGM) and the Fine-Grid Mesh (FGM), the latter being located over India and the surrounding oceans is shown in Figure 1. The horizontal resolutions of the CGM and the FGM are 1.5° and 0.5°, respectively. Envelope topography was obtained from the navy 10′ global topography data. Initial conditions were obtained from the European Centre for Medium Range Weather Forecast (ECMWF) analysis, available at 14 nonuniform vertical levels with 1.875° × 1.875° horizontal resolution. These data were interpolated to model grid points in the coarse-grid and fine-grid model. To achieve the objective of this study, numerical simulations were performed for 48 h starting at 12 UTC 16 July 1988.

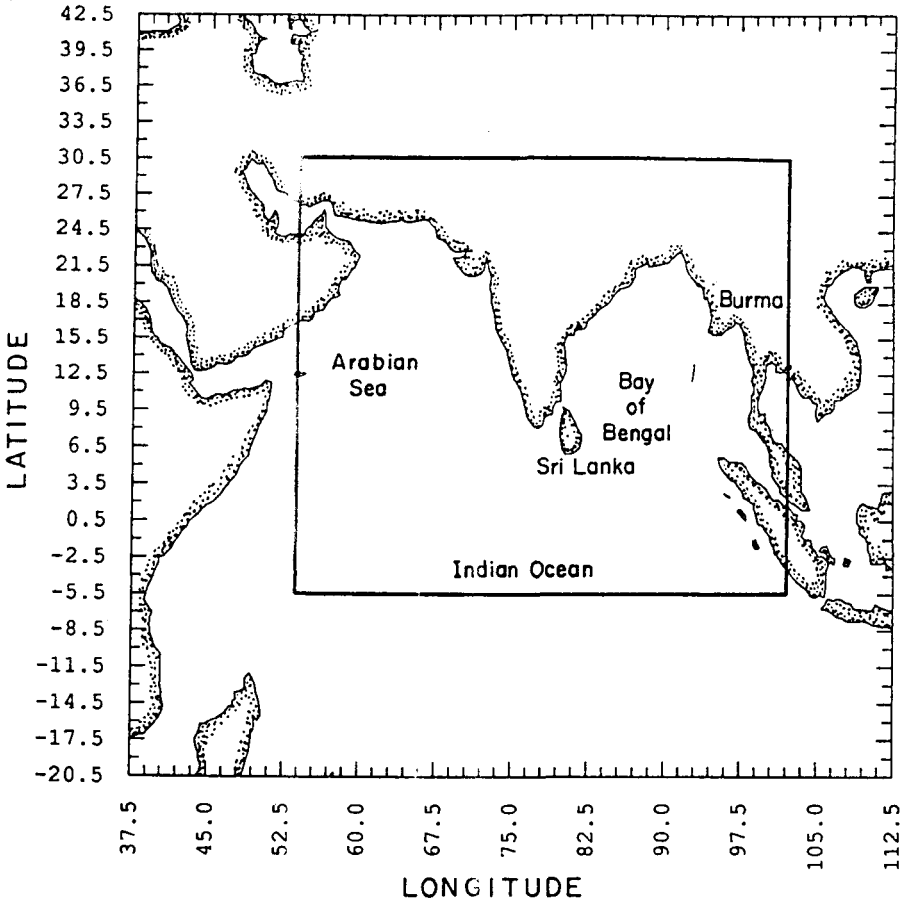

Fig. 1. The model domain of numerical simulation in the Coarse-Grid Mesh (CGM) and the Fine-Grid Mesh (FGM).

3. Synoptic Conditions

A monsoon depression was present over the Bay of Bengal close to the east coast of India during the simulation period (12 UTC 16 July to 12 UTC 18 July) and large rainfall rates were observed. Analyzed streamline distribution and horizontal winds for the 850 hPa at 12 UTC 16 July 1988 (initial conditions) are shown in Figure 2. Cyclonic circulations over the Bay of Bengal close to the east coast of India indicate the location of the monsoon depression. This depression moved northwest and made landfall during the next 24 h, moving farther inland to be centred over northeast India at 12 UTC 18 July. Large rainfall rates were reported over northeast India resulting from the monsoon depression. Along the west coast of India and offshore, large rainfall rates were also observed. The Somali jet, also

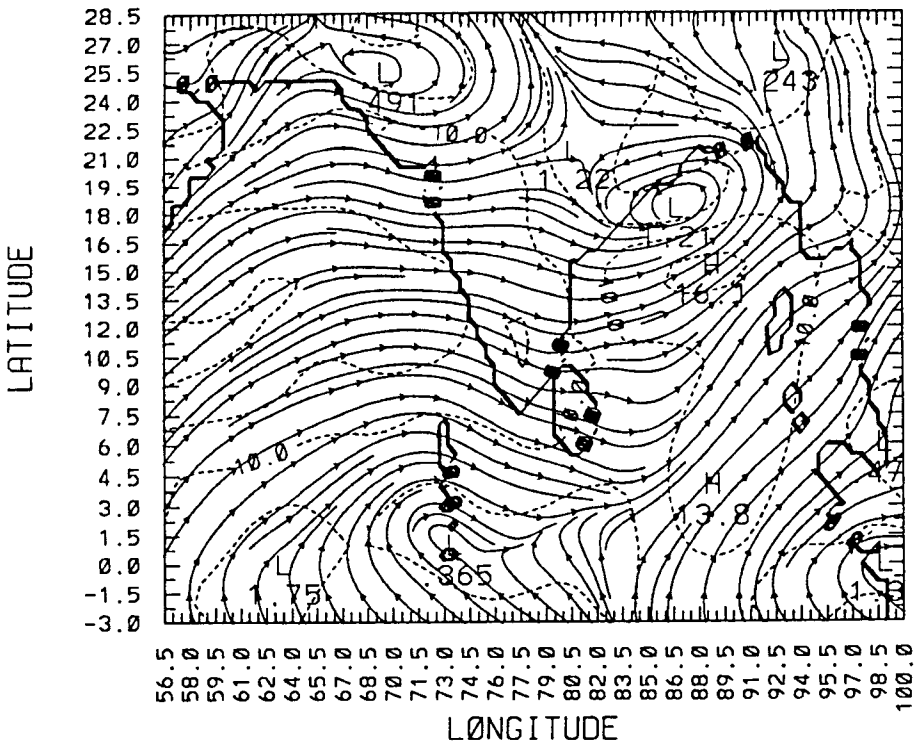

Fig. 2. Analyzed horizontal streamline and wind distribution at $\sigma = 0.85$ at 12 UTC 16 July 1988 (initial conditions). Contour interval is 5 m s^{-1}.

referred to as the east African Jet, is another feature present during the summer monsoon season. It is a low level jet situated at a height of about 1.5 km from the surface. Strong winds (broken lines in Figure 2 are isotachs) over the east coast of Africa are due to the presence of the Somali jet over this region. The interaction of the Somali jet with the monsoon circulation and its impact on the monsoon dynamics are still not well understood. Analyzed mean sea level pressure at 12 UTC 16 July 1988 indicated a low pressure center off the east coast of India consistent with the location of the cyclonic circulations seen in Figure 2. The low pressure center over west India is due to strong heating over the desert regions and is called the heat-low.

4. Discussion of Results

4.1. Structure of the monsoon boundary layer

A time-height section of the area-averaged winds for the region, 8° to 14° N and 60° to 67.5° E over the Arabian Sea is shown in Figure 3. The presence of the

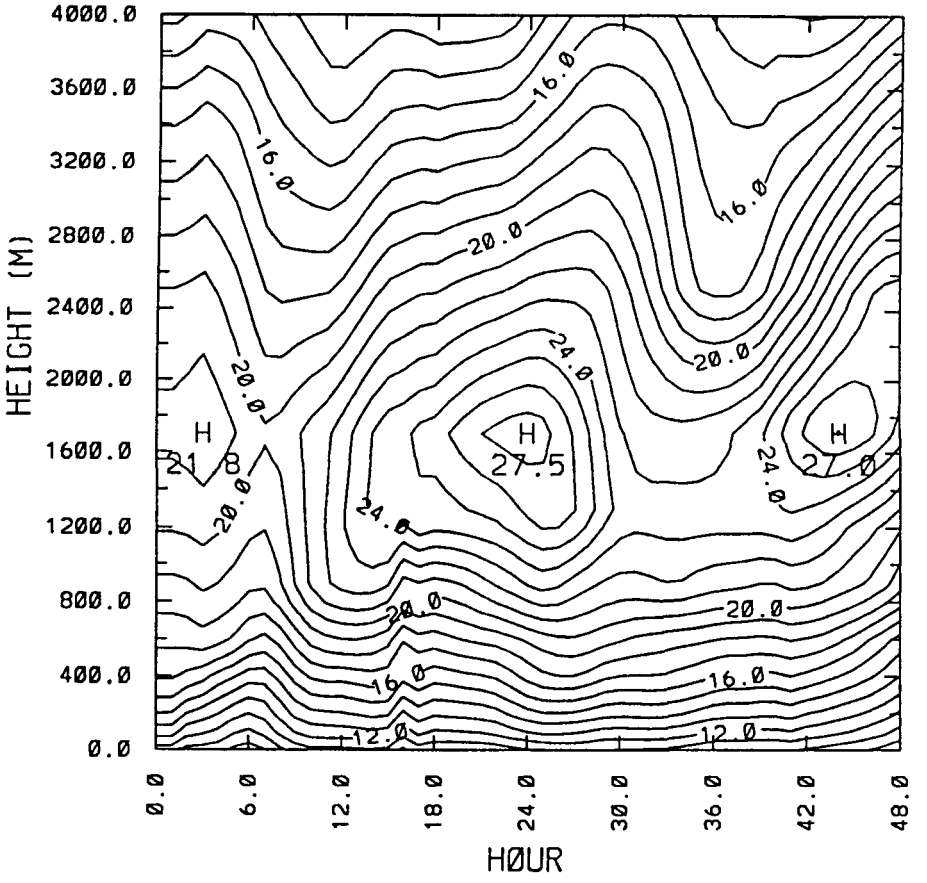

Fig. 3. Time-height section of area-averaged wind speed over the Arabian Sea for 48 h of simulation. Contour interval is 1 m s^{-1}.

Somali jet is indicated by the wind maximum at about 1600 m. During the period of simulation, the Somali jet showed a small diurnal variation. Wind speeds reached maximum values at the end of 23 h and 45 h of simulation which correspond to 1600 and 1400 LST. An observational study of the diurnal variation of the Somali jet over a land station Garissa, Kenya (0.5° S, 39.5° E) by Findlater (1966, 1969a, 1971a, 1974) revealed that the Somali jet attains its maximum speed by early morning, at 0500 GMT. Minimum speeds were observed during the afternoons, at about 1100 GMT, when surface heating is a maximum. Observations (Findlater, 1977) also indicate winds ranging from 25 to 50 m s^{-1} along the core of the Somali jet over the Arabian sea. Limited observational studies over the Arabian sea region indicate that there is a spatial variation of the height of the Somali jet and its intensity (Findlater, 1977; Holt and Raman, 1987), as found in the model predictions. But the diurnal variation can not be verified due to lack

of sufficient observations over the Arabian Sea. This diurnal variation in wind speed may be attributed to the response of the monsoon flow to the diurnal variations of the temperature contrasts between the Arabian sea and the Indian subcontinent. Predicted wind shear (Figure 3) is larger in the lower layers (below 1000 m) than aloft and the predicted height and magnitude of the wind speed maximum (27 m s^{-1}) in the Somali jet over the Arabian Sea are consistent with the observations (Holt and Raman, 1986). A latitude-height section of the predicted wind speeds along 68.5 °E also indicated a jet-like structure at an altitude of 1600 m between latitudes 9° N and 15° N. Elsewhere, over the ocean, predicted wind shear is weak.

Climatic sea surface temperatures (SSTs) for the month of July are used during the period of simulation. Over land, ground temperatures are prognostically determined using the surface energy budget. A time-height section of the area-averaged (8° to 14° N, 60° to 67.5° E) predicted virtual potential temperature over the western Arabian Sea is shown in Figure 4. A near-constant θ_v is predicted in the marine boundary layer indicating a mixed layer. In general, the area-averaged θ_v profile over the Arabian Sea indicates a boundary-layer height of about 800 m with a capping inversion in close agreement with the observations (Holt and Raman, 1987). The time-height section of the virtual potential temperature of the atmosphere predicted by the model over land indicated a strong diurnal variation in the boundary layer with a well-mixed layer during day time. The mixed-layer height ranged from 1000 m to 1800 m over land. Mixed-layer heights can also be inferred from the diurnal variation of TKE discussed in the following section.

4.2. Structure of the turbulence in the PBL

In order to determine the turbulence structure of the boundary layer, a time history of the turbulence kinetic energy (TKE) and its budget over a land station Bangalore (12.5° N, 78° E; hereafter referred to as BNG) are considered along with the area-averaged TKE budgets over the Western Arabian Sea (8° to 14° N, 60° to 67.5° E). Predicted TKE profiles for BNG at 1400 LST on the first and second days of simulations indicated a PBL height of between 1700 and 2100 m. There is some uncertainty (~400 m) about the exact height because of the coarse vertical resolution of the model at these altitudes.

The time-height section of the TKE predicted by the model for BNG is shown in Figure 5. During the two days of simulation, maximum TKE is predicted at 1500 LST (22 and 46 h) with a magnitude of about 0.92 $m^2 s^{-2}$ for the first day and 1.12 $m^2 s^{-2}$ for the second day. Since there is a strong diurnal variation over the land, there is a significant change in the TKE from early morning (0200 UTC) to the afternoon (0800 UTC). During night time, the stable boundary-layer height is only about 100–250 m compared to a daytime convective boundary-layer height of ~1800 m. Also, during the night time there is little variation with time in boundary-layer height, which is consistent with the generally observed pattern over land (Stull, 1989). At 1500 LST, for the second day of simulation, turbulence

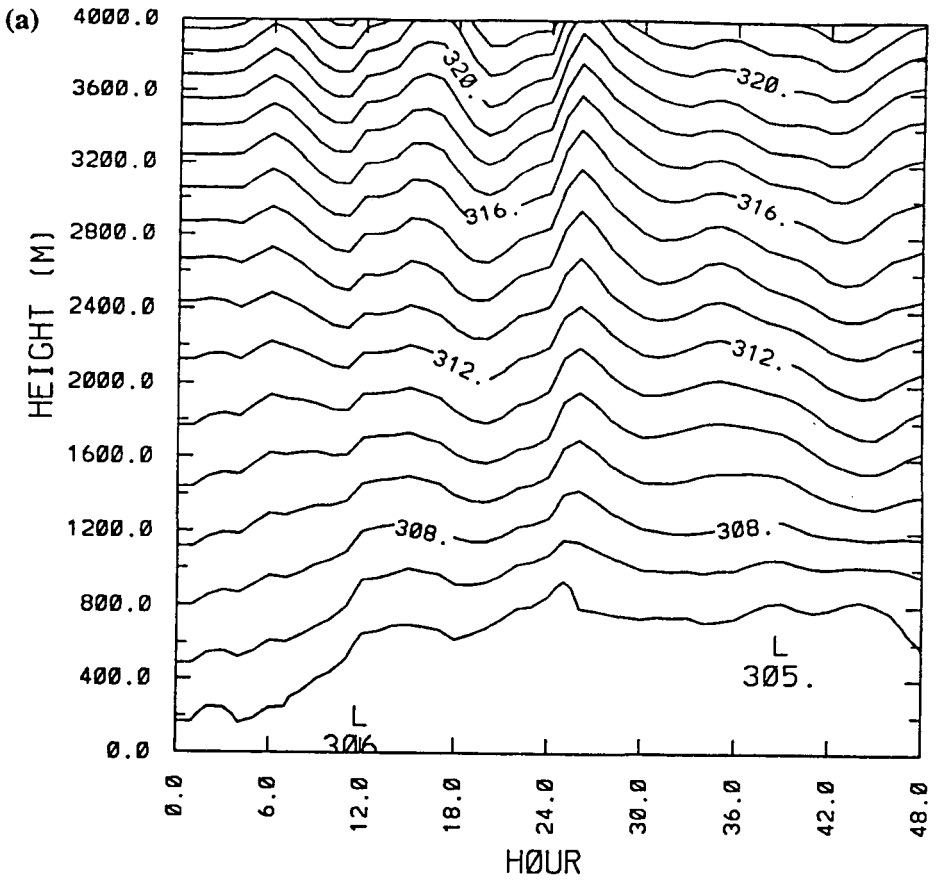

Fig. 4. Time-height section of area-averaged virtual potential temperature over the Arabian Sea. Contour interval is 1 °K.

kinetic energy in the lowest layers has increased as compared to the previous day, accompanied by a small increase in PBL height. Observations of the height of the boundary layer for the present period of simulation are not available but a height of about 1000 m was observed during the 1987 monsoon over this region (Raman *et al.*, 1990). We believe that the relatively larger boundary-layer heights predicted by the model may be due to the neglect of soil moisture and evaporation over land. In the present model, surface hydrology is not considered and a dry soil with an albedo of 0.28 is assumed. Observational studies of boundary-layer heights during active and break monsoon periods (Kusuma *et al.*, 1991) also indicate that soil moisture depletion is one of the factors contributing to the increase in boundary-layer heights. A day-to-day variation in the height of the nocturnal boundary layer was also found.

Predicted vertical profiles of the TKE budget for BNG at 1400 LST and 0200

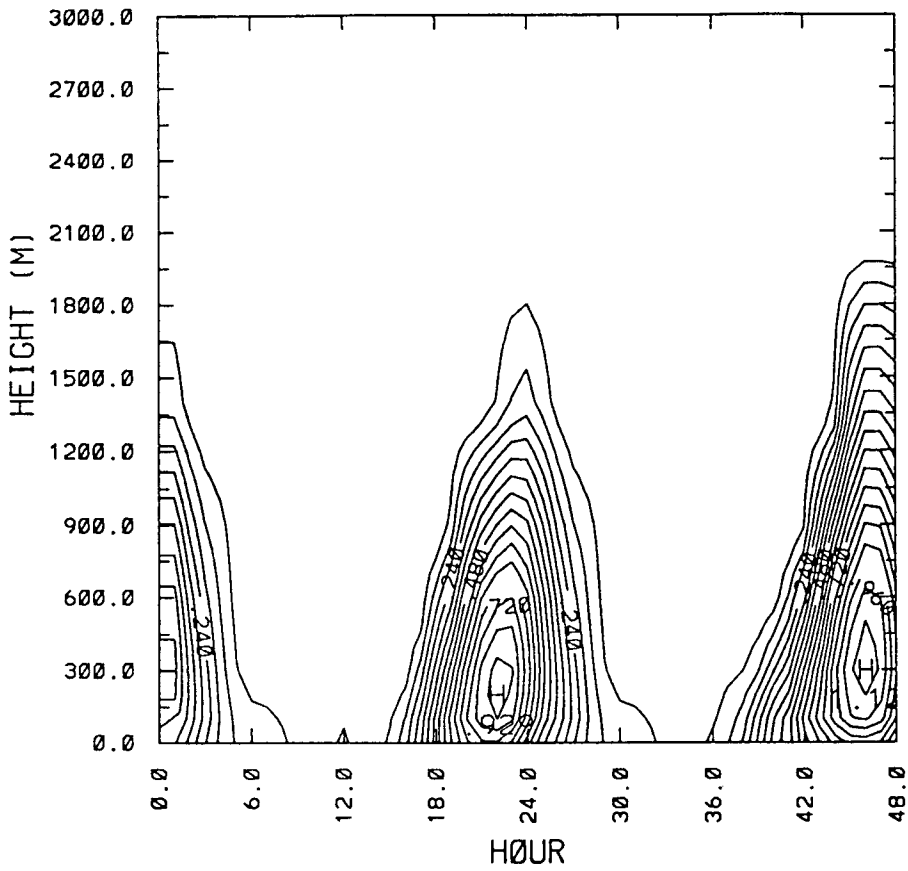

Fig. 5. Time-height section of turbulent kinetic energy over a land station (Bangalore) for 48 h of simulation. Contour interval is 0.06 $m^2 s^{-2}$.

LST for the first day of simulation are shown in Figure 6a and 6b, respectively. Except near the surface, the buoyancy production term (denoted by B) is the major source term and the shear production term (denoted by A) is the secondary source term for generation of turbulence; the primary sink is the dissipation term (denoted by D). The turbulence transport term (denoted by C) is a secondary sink in the lower layers of the boundary layer. At altitudes of 500 m and above, the shear production term becomes negligible. Above 1200 m, the buoyancy production term becomes negative because of entrainment of air from the free atmosphere. The turbulence transport term becomes a source term above 900 m. Also, the dissipation term becomes small in these layers. The small imbalance term (denoted by E) is believed to be primarily due to the neglect of pressure transport and advection of turbulence. During the night time (Figure 6b), the major source for turbulence is the shear production term (denoted by A) while the buoyancy

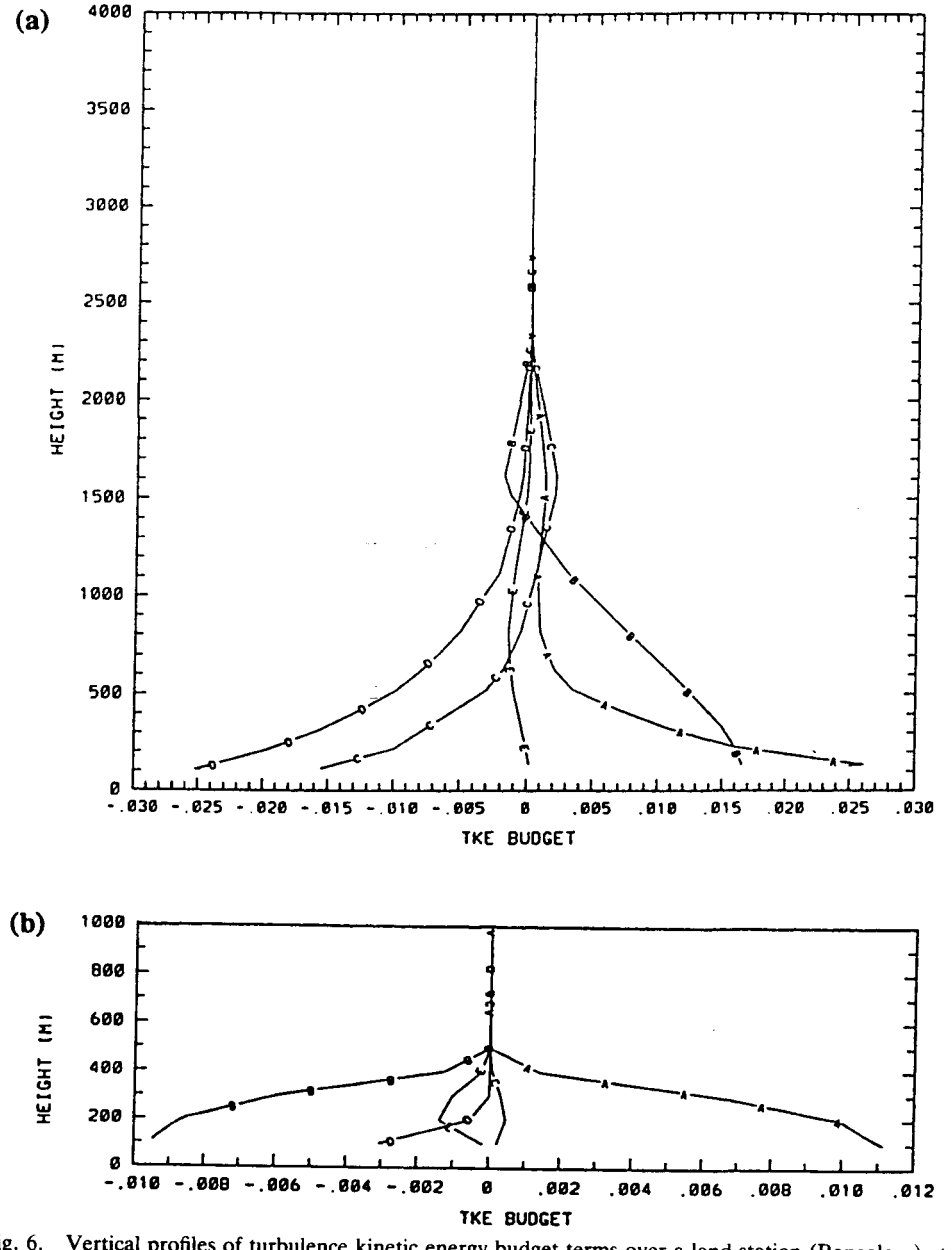

Fig. 6. Vertical profiles of turbulence kinetic energy budget terms over a land station (Bangalore) at (a) 14 LST, and (b) 02 LST for day 1. Shear production A, Buoyancy production B, Transport C, Dissipation D and the Imbalance E.

term is the major sink term (denoted by B). Contrary to the daytime TKE budget, dissipation (denoted by D) is a smaller sink term.

The time-height section of the area-averaged TKE over the Arabian Sea (8° to 14° N, 60° to 67.5° E) is shown in Figure 7a. Major differences from the land site

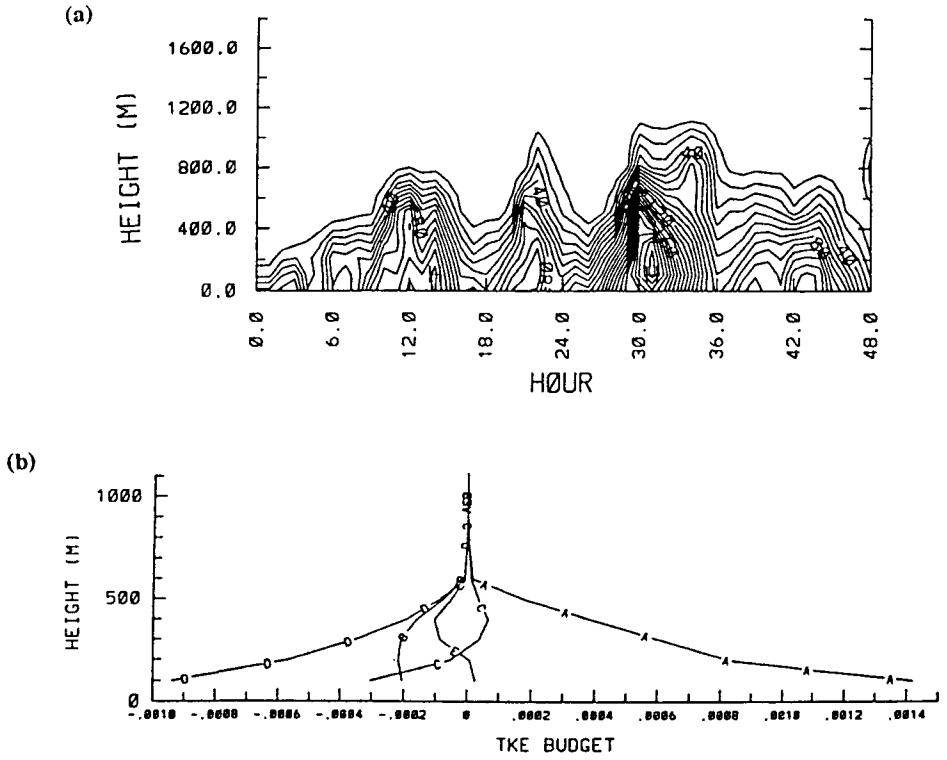

Fig. 7. (a) Time-height section of area-averaged turbulence kinetic energy over the Arabian Sea (8° to 14° N, 60° to 67.5° E) for 48 h of simulation. Contour interval is $1.0 \times 10^{-3}\,m^2\,s^{-2}$. (b) Vertical profiles of area-averaged turbulent kinetic energy budget terms over the Arabian Sea (8° to 14° N, 60° to 67.5° E) at 14 LST for day 1. Shear production A, Buoyancy production B, Transport C, Dissipation D and the Imbalance E.

are the lack of a strong diurnal variation and somewhat lower values of TKE. The maximum value of the TKE predicted by the model over this region is $\sim 0.015\,m^2\,s^{-2}$ compared to $0.88\,m^2\,s^{-2}$ over land. Area-averaged TKE budget profiles over this region at 1400 LST of the first day of simulation are shown in Figure 7b. Near-neutral to slightly stable conditions are predicted over this region. Buoyancy production is a minor sink term for TKE in the lower layers. Shear production is the major source of TKE which gradually decreases with height. The dissipation and buoyancy terms are major sinks in the lower layers over this region, in the upper layers, the transport term is a secondary source term for TKE. The imbalance term (denoted by E) is small. Temporal variation of area-averaged TKE over the Bay of Bengal region (not shown) is somewhat similar to that over the Arabian Sea except that the magnitudes are slightly (about 5 to 10%) smaller. This may be partly due to the presence of a monsoon depression over the Bay of Bengal causing strong winds over this region. The maximum height of the area-averaged marine boundary layer over the Bay of Bengal is

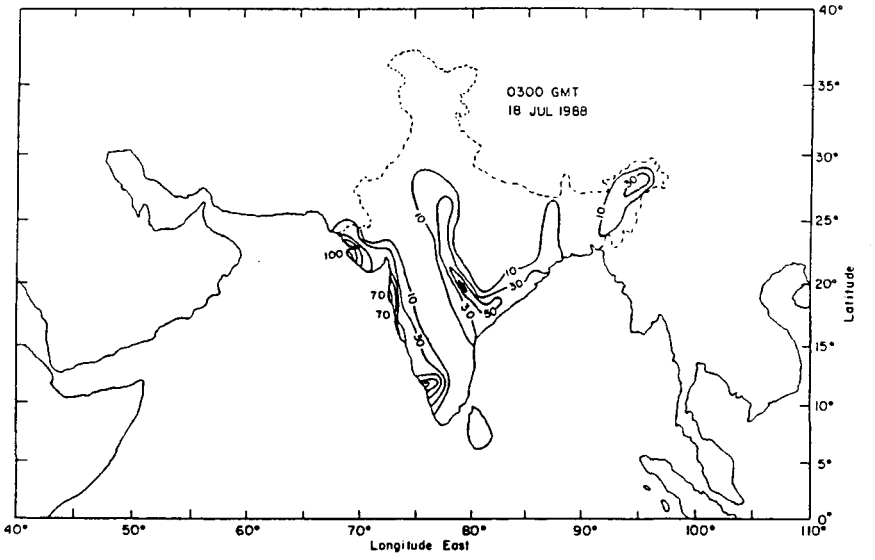

Fig. 8. Observed rainfall rates for a period of 24 h ending at 03 UTC 18 July 1988.

about 1000 m. The vertical profiles of area-averaged TKE budgets for this region are also somewhat similar to that over the Arabian Sea. The mean θ_v profile over this region indicates that the boundary layer is stable.

4.3. Dynamics of the monsoon

Observations indicated that the monsoon was active during July 1988 with large rainfall rates (about 100 to 200 mm d^{-1}). Along the west coast of India, observed rainfall was due to the orographic-convective processes while over central India it was due to a monsoon depression. At 12 UTC 16 July 1988, a monsoon depression was located offshore of the east coast of India. During the next 24 h, the monsoon depression made landfall, leading to large rainfall rates of about 100 to 160 mm d^{-1} over the central and east coast of India. During the next 24 h, the monsoon depression moved northwest and produced rainfall over this region (Figure 8). For these two days, observations also indicated rainfall rates of about 100–200 mm d^{-1} along the west coast of India. Observations indicate that a preferred location of the rainfall maximum is offshore (Ramakrishnan and Gopinatha Rao, 1958; Ramachandran, 1972). There was a considerable spatial and temporal variation of rainfall during the 1979 monsoon season with a maximum rate of ~200 mm d^{-1} over the Arabian Sea off the west coast of India (Krishnamurti *et al.*, 1983).

As expected, increased horizontal resolution in the FGM resulted in the prediction of higher rainfall rates than that in the CGM. Also, the spatial distribution of rainfall associated with the monsoon depression is predicted better by the FGM.

For the first day of simulation, the rainfall maximum (not shown) over the Bay of Bengal over the east coast of India was about 100 mm d^{-1}, about two times higher than that in the CGM and comparing well with observations. Along the west coast of India, the predicted rainfall was about 117 mm d^{-1} with the maximum located just offshore.

Predicted rainfall for the CGM during the second day of simulation ending at 12 UTC 18 July is shown in Figure 9a. At this time, the monsoon depression is located over northeast India, producing heavy rainfall. Rainfall over this region for the second day is larger compared to that during the first day of simulation. Along the west coast of India, the spatial distribution of rainfall is somewhat similar to that during the previous day for the CGM. However, the rainfall maximum offshore of the west coast of India is again consistent with the observations. Predicted rainfall for the FGM during the second day of simulation ending at 12 UTC 18 July is shown in Figure 9b. As can be seen from the observations (Fig. 8), a rainfall band along the monsoon trough over central India is again well predicted. Along the west coast of India, the predicted rainfall maximum is just offshore with a rate of about 202 mm d^{-1}. In general, predicted rainfall and its spatial distribution for the FGM are in better agreement with the observations than those for the CGM. For both days, the model-predicted grid-scale (large-scale) rainfall is much less than the subgrid-scale (convective) rainfall except over the high elevation mountains. Near the Western Ghats region, grid-scale rainfall is negligible, indicating that most of the rainfall over this region is from deep convection.

Latent heat fluxes from the surrounding oceans for the first and the second simulation day are shown in Figures 10a and 10b, respectively. The spatial distribution of latent heat fluxes reflects the low level flow pattern. Latent heat fluxes indicate maximum values offshore of the east coast of Africa and over the central Arabian Sea due to the presence of stronger winds. Latent heat fluxes for the second day of simulation (Figure 10b) indicate similar features as found during the first day but with greater magnitudes. Latent heat fluxes over the southern Indian Ocean are larger than those during the first day. The maximum value of latent heat fluxes over the Arabian Sea was about 187 W m^{-2}, comparable to the observed value of 200 W m^{-2} for the 1979 monsoon (Holt and Raman, 1985). Predicted latent heat fluxes over the Indian Ocean (closer to the southern boundary) were about 50 to 150 W m^{-2} and estimated latent heat fluxes (Simon and Desai, 1991) over this region during the MONEX79 indicate similar values (50 to 200 W m^{-2}).

In order to compare predicted wind fields for most of the monsoon region to those in the analyzed data, model predictions for the CGM are considered. Latitude-height section of zonally averaged zonal winds obtained from analysis for the CGM at 12 UTC 18 July is shown in Figure 11a. One of the distinct features in the flow pattern is the presence of a low level wind maximum between 6.5° and 18.5° N, indicating the observed location of the Somali jet at 1.5 km. The wind

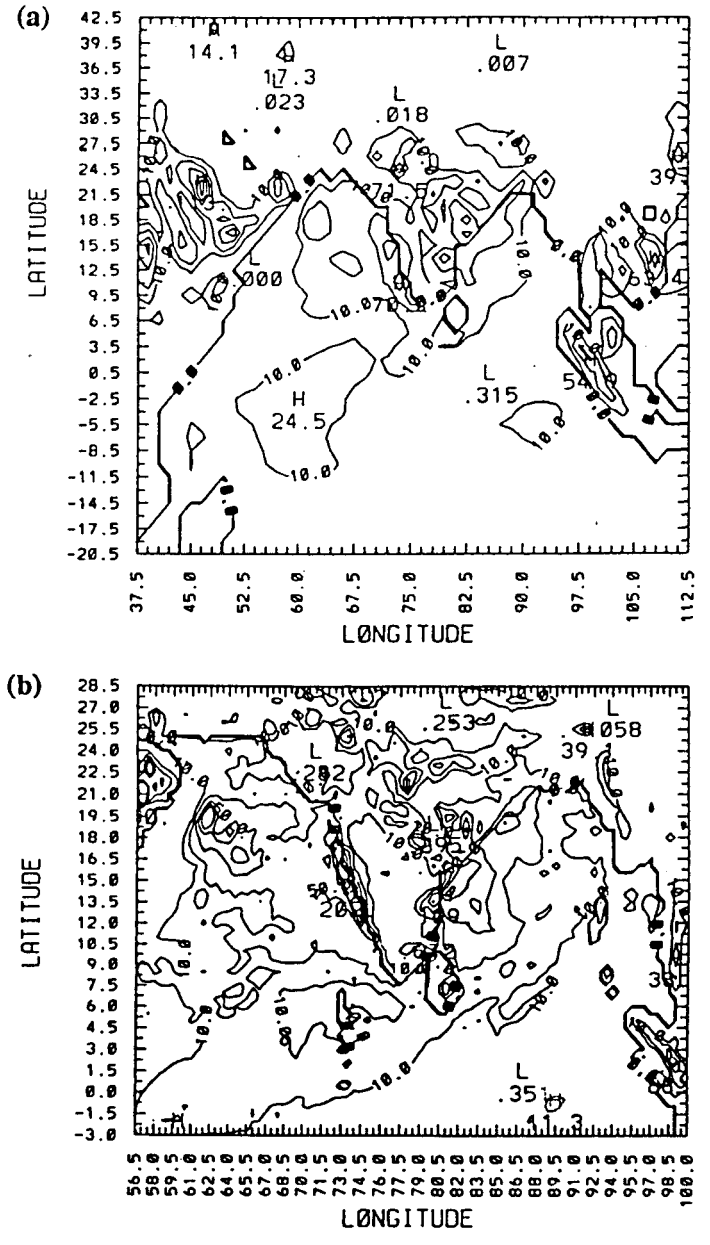

Fig. 9. The model predicted rainfall for a period of 24 h ending at 12 UTC 18 July 1988 (a) for the CGM domain and (b) for the FGM domain, respectively. Contour intervals are 10, 20, 50, 80, 100, 125 and 10, 25, 50, 75, 100, 125 mm d^{-1}.

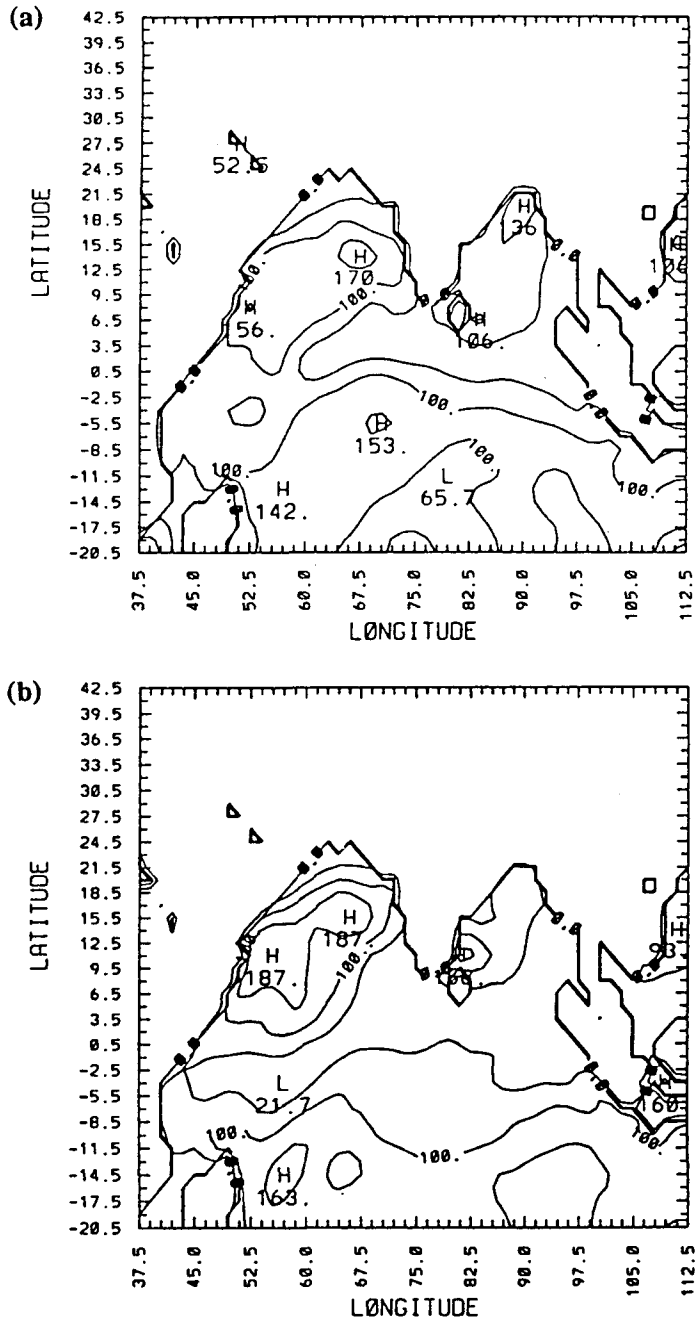

Fig. 10. Predicted latent heat fluxes at the end of (a) 24 h, and (b) 48 h of simulation. Contour interval is 50 W m^{-2}.

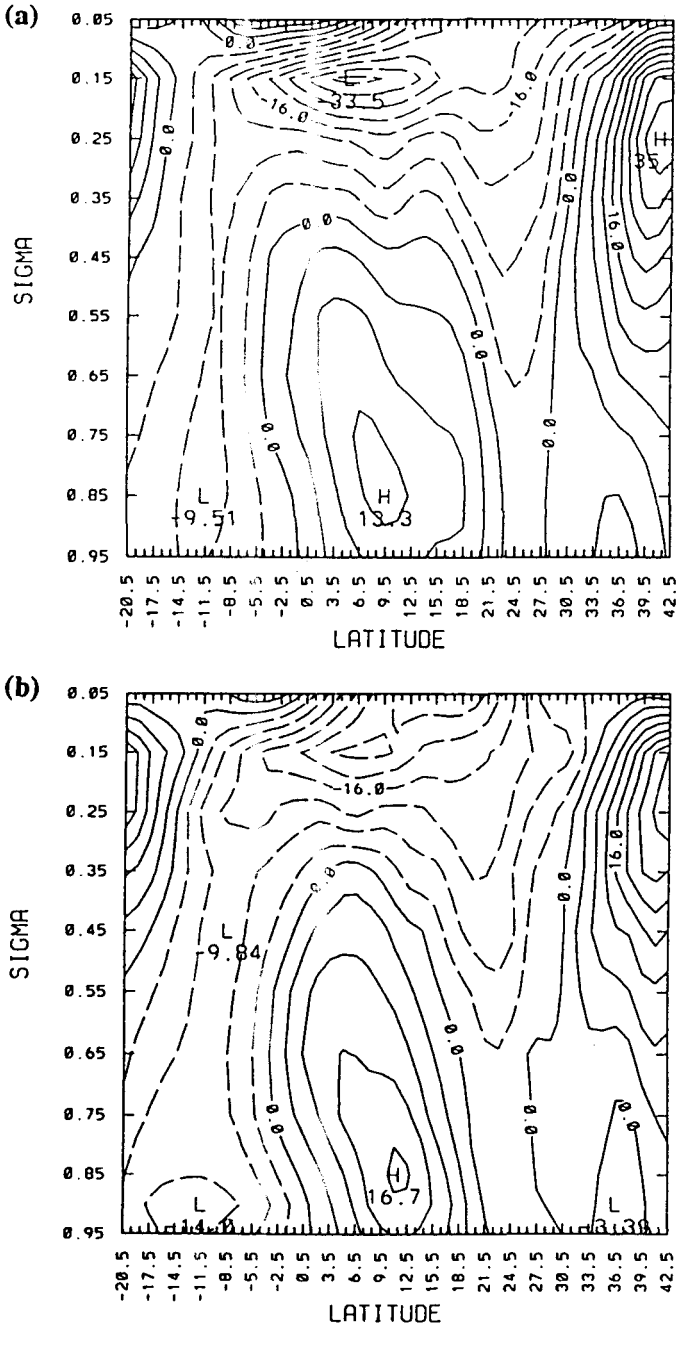

Fig. 11. Latitude-height section of zonally averaged zonal winds for the CGM at 12 UTC 18 July from (a) the analysis, and (b) from the model predictions. Contour inteval is 4 m s^{-1}.

maximum at upper levels (at 0.15σ) is due to the presence of a tropical easterly jet. It can be seen that there exists a strong vertical wind shear from the lower to the upper troposphere over this region. Wind maxima on the left and right side boundaries of Figure 11a are due to the presence of subtropical westerly jets in the southern and northern hemispheres, respectively. Corresponding latitudinally averaged zonal winds from the model predictions are shown in Figure 11b. The predicted Somali jet is stronger than that in the analysis while the easterly jet is weaker. Subtropical westerly jets over both hemispheres are simulated well.

5. Conclusions

A nested grid mesoscale model with a TKE turbulence closure scheme is used to simulate the atmospheric processes during an active monsoon period. As expected, the diurnal variation of boundary-layer height over land is significant whereas over the oceans, the height of the boundary layer does not vary very much. The monsoon depression is reasonably well simulated and the predicted spatial distributions of winds, rainfall, and latent heat fluxes are close to observed ones. The main features associated with the monsoon circulations such as the Somali jet and monsoon depression are well predicted and are in good agreement with the observations. The spatial distribution of the predicted rainfall and the location of a maximum off the west coast of India are in agreement with the observed ones. Prediction of relatively deeper boundary layers over the land compared to observations may be due to the neglect of surface hydrological processes. Inclusion of evaporation from the land surface may improve model predictions. Our future research will involve inclusion of diabatic initialization and the physics related to surface hydrological processes, and atmospheric radiation in the model.

Acknowledgements

The authors would like to acknowledge assistance provided by Dr. Teddy Holt during the model development. This work was supported in part by the Naval Research Laboratory and by the Division of International Programs, National Science Foundation by Grant INT-9008926. Computer resources were provided by the North Carolina Supercomputing Center, Research Triangle Park, NC.

References

Anthes, R. A.: 1977, 'A Cumulus Parameterization Scheme Utilizing a One-Dimensional Cloud Model', *Mon. Wea. Rev.* **105**, 207–286.

Blackadar, A. K: 1976, 'Modeling the Nocturnal Boundary Layer', Preprints, *Third Symposium on Atmospheric Turbulence, Diffusion and Air Quality*, Raleigh, Amer. Meteor. Soc., pp. 46–49.

Businger, J. A.: Wyngaard, J. C., Izumi, Y., and Bradley, E. F., 1971, 'Flux-Profile-Relationship in the Atmospheric Surface Layer', *J. Atmos. Sci.* **28**, 181–189.

Chang, S. W.: 1979, 'An Efficient Parameterization of Convective and Non-Convective Planetary Boundary Layers for Use in Numerical Models', *J. Appl. Meteoro.* **18**, 1205–1215.

Chang, S. W.: 1981, 'Test of a Planetary Boundary Layer Parameterization Based on a Generalized Similarity Theory in Tropical Cyclone Models', *Mon. Wea. Rev.* **109**, 843–853.

Davies, H. C.: 1976, 'A Lateral Boundary Formulation for Multi-Level Prediction Models', *Quart. J. Roy. Meteorol. Soc.* **102**, 405–418.

Davies, H. C.: 1983, 'Limitations of Some Common Lateral Boundary Schemes Used in Regional NWP Models', *Mon. Wea. Rev.* **111**, 1002–1012.

Deardorff, J. W.: 1980, 'Stratocumulus-Capped Mixed Layers Derived from a Three-Dimensional Model', *Boundary-Layer Meteorol.* **18**, 495–527.

Deterling, H. W. and Etling, D.: 1985, 'Application of E-e Turbulence Model to the Atmospheric Boundary Layer', *Boundary-Layer Meteorol.* **33**, 113–133.

Gerber, H., Chang, S. and Holt, T.: 1989, 'Evolution of a Marine Boundary Layer Jet', *J. Atmos. Sci.* **46**, 1312–1326.

Gronas, S., Foss, A. and Lystad, M.: 1987, 'Numerical Simulations of Polar Lows in the Norwegian Sea', *Tellus* **39A**, 334–353.

Grossman, R. L., and Durran, D. R.: 1984, 'Interaction of Low-Level Flow with the Western Ghat Mountains and Offshore Convection in the Summer Monsoon', *Mon. Wea. Rev.* **112**, 652–672.

Holt, T., and Raman, S.: 1985, 'Aircraft and Ship Observations of the Mean Structure of the Marine Boundary Layer over the Arabian Sea during MONEX 79', *Boundary-Layer Meteorol.* **33**, 259–282.

Holt, T. and Raman, S.: 1987, 'A Study of Mean Boundary-Layer Strucutres over the Arabian Sea and the Bay of Bengal During Active and Break Monsoon Periods', *Boundary-Layer Meteorol.* **38**, 73–94.

Holt, T. and Raman, S.: 1988, 'A Review and Compariative Evaluation of Multilevel Boundary Layer Parameterizations for First-Order and Turbulent Kinetic Energy Closure Schemes', *Reviews Geophys.* **26**, 761–780.

Holt, T., Chang, S., and Raman, S., 1990: 'A Numerical Study of the Coastal Cyclogenesis in GALE IOP 2: Sensitivity to PBL Parameterizations', *Mon. Wea. Rev.* **118**, 234–257.

Huang, C. Y. and Raman, S.: 1989, 'Numerical Simulations of Cold Air Advection over the Appalachian Mountain and the Gulf Stream', *Mon. Wea. Rev.* **118**, 343–362.

Krishnamurti, T. N., Cocke, S., Pasch, R., and Low-Nam, S., 1983: 'Precipitation Estimates from Rainguage and Satellite Observations: Summer MONEX', Dept. of Meteorology, Florida State University, 377 pp.

Kuo, H. L.: 1974, 'Further Studies of the Parameterization of the Influence of Cumulus Convection on Large-Scale Flow', *J. Atmos. Sci.* **31**, 1232–1240.

Kusuma, G. R., Raman, R., and Prabhu, A., 1991: 'Boundary-Layer Heights over the Monsoon Through Region During Active and Break Phases', *Boundary-Layer Meteorol.* **57**, 129–138.

Madala, R. V., Chang, S. W., Mohanty, U. C., Madan, S. C., Paliwal, R. K., Sarin, V. B., Holt, T., and Raman, S.: 1987, 'Description of the Naval Research Laboratory Limited Area Dynamical Weather Prediction Model', NRL Memo. Rep., No. 5992, Naval Research Laboratory, Washington, D.C., 131 pp.

Monin, A. S. and Yaglom, A. M.: 1971, *Statisticalf Fluid Mechanics. Vol. I*, MIT Press, 468–504.

Raman, S., Templeman, B., Templeman, S., Holt, T., Murthy, A. B., Singh, M. P., Agarwaal, P., Nigam, S., Prabhu, A., and Ameenullah, S.: 1990, Structure of the Indian Southwesterly Premonsoon and Monsoon Boundary Layers: Observations and Numerical Simulation', *Atmos. Env.* **24A**, 723–734.

Seller, W. D., 1965, *Physical Climatology*, University of Chicago Press, 53–54.

Simon, B., and Desai, P. S.: 1991, 'Estimation of Heat Fluxes over Indian Ocean using Satellite Data', *Indo-US Seminar on Parameterization of Sub-grid Scale Processes in Dynamical Models of Medium Range Prediction and Global Climate.* IITM, Pune, India, 193–99.

Stull, R. B.: 1989: *An Introduction to Boundary Layer Meterology*, Kluwer Academic Publishers, 666 pp.

Sun, W. Y. and Hsu, W. R.: 1988, 'Numerical Study of a Cold Air Outbreak over the Ocean', *J. Atmos. Sci.* **45**, 1205–1227.

Yamada, T. and Mellor, G.: 1975, A Simulation of Wangara Atmospheric Boundary Layer Data', *J. Atmos. Sci.* **12**, 2309–2329.